Evaluation of renal metabolic response to partial ureteral obstruction with hyperpolarized ^{13}C MRI

David J. Niles[1], **Jeremy W. Gordon**[1], **Gengwen Huang**[2], **Shannon Reese**[3], **Erin B. Adamson**[1], **Arjang Djamali**[3,4], and **Sean B. Fain**[1,4]

[1]Medical Physics, University of Wisconsin–Madison, Madison, WI, USA

[2]Surgery, University of Wisconsin–Madison, Madison, WI, USA

[3]Medicine, Nephrology, University of Wisconsin–Madison, Madison, WI, USA

[4]University of Wisconsin School of Medicine and Public Health, Madison, WI, USA

Abstract

Hyperpolarized ^{13}C magnetic resonance imaging (MRI) may be used to non-invasively image the transport and chemical conversion of ^{13}C–labeled compounds *in vivo*. In this study, we utilize hyperpolarized ^{13}C MRI to evaluate metabolic markers in the kidneys longitudinally in a mouse model of partial unilateral ureteral obstruction (pUUO). Partial obstruction was surgically induced in the left ureter of nine adult mice, leaving the right ureter as a control. ^{1}H and hyperpolarized [1-^{13}C]pyruvate MRI of the kidneys was performed 2 days prior to surgery (baseline) and at 3, 7 and 14 days post-surgery. Images were evaluated for changes in renal pelvis volume, pyruvate, lactate and the lactate to pyruvate ratio. After 14 days, mice were sacrificed and immunohistological staining of both kidneys for collagen fibrosis (picrosirius red) and macrophage infiltration (F4/80) was performed. Statistical analysis was performed using a linear mixed effects model. Significant kidney × time interaction effects were observed for both lactate and pyruvate, indicating that these markers changed differently between time points for the obstructed and unobstructed kidneys. Both kidneys showed an increase in the lactate to pyruvate ratio after obstruction, suggesting a shift towards glycolytic metabolism. These changes were accompanied by marked hydronephrosis, fibrosis and macrophage infiltration in the obstructed kidney, but not in the unobstructed kidney. Our results show that pUUO is associated with increased pyruvate to lactate metabolism in both kidneys, with injury and inflammation specific to the obstructed kidney. The work also demonstrates the feasibility of the use of hyperpolarized ^{13}C MRI to study metabolism in renal disease.

Correspondence: S. Fain, Department of Medical Physics, 1111, Highland Ave., 1133 Wisconsin Institutes for Medical Research, University of Wisconsin–Madison, Madison, WI 53705, USA., sfain@wisc.edu.
ORCID
David J. Niles http://orcid.org/0000-0002-1989-4505
Jeremy W. Gordon http://orcid.org/0000-0003-2760-4886
Sean B. Fain http://orcid.org/0000-0001-5461-0646

1 INTRODUCTION

Urinary tract obstruction (UTO) impairs the flow of urine and, left untreated, may lead to irreversible kidney damage. Congenital UTO in children is particularly concerning, as it is the second most common cause of pediatric renal transplant, accounting for 15.3% of cases.[1] The factors which contribute to congenital UTO are not well understood, and the pathogenesis is heterogeneous. This leads to varying approaches to clinical management. Watchful waiting is appropriate for some patients, as hydronephrosis may resolve spontaneously in many cases. However, others require surgical intervention, and prognostic markers indicating the best course of action are generally lacking. Improved methods of assessment are needed to guide congenital UTO management.

UTO is commonly studied in so-called unilateral ureteral obstruction (UUO) animal models, which involve ligation of one ureter whilst leaving the other as a control.[2] Obstruction may be complete or partial, with the latter more closely mimicking UTO in humans. Obstructed kidneys in UUO models are characterized by interstitial fibrosis, infiltration by macrophages, reduced renal blood flow and glomerular filtration, and reduced ability to concentrate urine.

Amongst other aspects of UTO, there is interest in understanding the metabolic changes involved, and a number of metabolomic studies have found altered metabolite profiles in urine or serum associated with obstructive renal injury. Yoshioka et al.[3] found changes in fatty acid composition in the urine of UUO rats. MacLellan et al.[4] observed a reduction in compounds associated with oxidative phosphorylation in UUO rats, implying the impairment of aerobic metabolism. Changes in serum metabolites post-UUO were also observed by Zhang et al.[5] Finally, Dong et al.[6] reported changes in the level of several metabolites in humans with UTO following relief of obstruction.

Hyperpolarized ^{13}C magnetic resonance imaging (MRI) enables real-time imaging of transport and regional metabolic processes *in vivo*. This technology may contribute to our understanding of the metabolic changes associated with UTO in both the obstructed and unobstructed contra-lateral kidneys with the potential to aid in clinical management as a method of monitoring UTO progression or resolution. The kidney is well suited for hyperpolarized ^{13}C MRI because of its large blood supply and high rates of both aerobic and anaerobic metabolism, and renal applications of the method have been a focus of several recent studies.[7–14] However, hyperpolarized ^{13}C MRI is entirely unexplored in the context of UTO despite the recognition that metabolic markers are associated with the disease. Moreover, the possible shift to glycolytic metabolism observed further suggests that hyperpolarized [1-^{13}C]pyruvate conversion to lactate may be a useful marker that is sensitive to the disease process. The purpose of this study was to use hyperpolarized [1-^{13}C]pyruvate MRI to observe the metabolic response to kidney injury longitudinally in a partial UUO (pUUO) mouse model using pyruvate to lactate dynamics.

2 EXPERIMENTAL DETAILS

2.1 Animal handling and pUUO surgery

All experiments complied with the policies of our institution's Animal Care and Use Committee and were conducted using approved animal use protocols. This study included nine healthy male FVB mice (mean, 25.1 g; 9–15 weeks of age). Partial obstruction of the left ureter was performed surgically by a trained microsurgeon (2+ years of experience) under 1–3% isoflurane anesthesia. After a small incision along the midline of the abdomen, the left ureter was exposed by blunt dissection. A short segment of suture was positioned alongside the ureter, and the ureter and suture were ligated. After ligation, the segment of suture was removed, allowing the ureter to expand to a partially obstructed diameter. This method for partial obstruction has been validated on the basis of immunohistological staining for renal fibrosis, which showed a level intermediate between that of unobstructed and completely obstructed ureters (data not shown).

2.2 Image acquisition

Imaging of the kidneys was performed on a 4.7-T small animal system (Agilent Technologies, Palo Alto, CA, USA) using a single-channel, dual-tuned $^1H/^{13}C$ volume coil (Doty Scientific, Columbia, SC, USA). Mice were fasted overnight for at least 10 h prior to imaging in metabolic cages. Mice were imaged under isoflurane anesthesia (1.5% in 100% O_2) at four time points: 2 days prior to surgery (baseline) and 3, 7 and 14 days post-surgery (Figure 1). Mouse internal temperature was monitored continuously during imaging and maintained above 36°C using a warm air blower (Small Animal Instruments, Inc., Stony Brook, NY, USA).

Anatomic ^1H images were acquired using a T_1-weighted three-dimensional (3D) spoiled gradient echo sequence (SPGR) and a T_2-weighted two-dimensional (2D) fast spin echo (FSE) sequence. The 3D SPGR images were used for volumetric measurement of the kidneys, whereas the 2D FSE images provided favorable contrast for anatomic visualization. The 3D SPGR parameters were as follows: TR = 4.36 ms; TE = 2.2 ms; flip angle, 20°; bandwidth, 100 kHz; number of averages, 3; image dimensions, $80 \times 40 \times 40$ mm^3; spatial resolution, 0.31 mm isotropic; scan duration, 3.5 min. The 2D FSE parameters were as follows: TR = 3500 ms; TE = 20 ms; echo train length, 8; effectiveTE, 66 ms; bandwidth, 100 kHz; number of averages, 8; field of view, 32×32 mm^2; slice thickness, 2 mm; in-plane spatial resolution, 0.25 mm; scan duration, 7.5 min. A B_0 field map in the axial plane was calculated with images acquired at five TEs using a 2D SPGR sequence, as follows: TR = 11.5 ms; TE = 4.2–7.0 ms; echo spacing, 0.4 ms; flip angle, 20°; bandwidth, 50 kHz; number of averages, 8; field of view, 64×64 mm^2; slice thickness, 2 mm; in-plane spatial resolution, 0.25 mm; scan duration, 3.1 min.

Dynamic hyperpolarized ^{13}C imaging was performed on a single 10-mm axial slice spanning both kidneys. Data were acquired at 32 time points using a single-shot uniform-density spiral SPGR sequence. Data were acquired at five TEs and time points were separated by ~5 s for a total scan duration of 2.7 min. Additional parameters included: TR = 55 ms; TE = 0.25–5.01 ms; echo spacing, 1.19 ms; flip angle, 10°; bandwidth, 250 kHz;

field of view, 64×64 mm^2; reconstructed in-plane spatial resolution, 2 mm. The spiral acquisition was started just prior to a 3-s injection of hyperpolarized [1-^{13}C]pyruvate (100mM; volume, 10 μL/g) via the tail vein. A ^{13}C spectrum (flip angle, 5°) over the imaging slice was acquired between each time point in order to measure the chemical shift of metabolites. The *k*-space trajectory of the spiral readout was measured separately with a small phantom, using a thin-slice excitation method.[15,16]

2.3 Biochemical analysis

2.3.1 Sample collection—Urine and blood samples were collected from each mouse at baseline, day 3, day 7 and day 14. Urine samples were collected using metabolic cages during overnight fasting. Blood samples were collected under anesthesia after imaging via the retro-orbital plexus. Following imaging at day 14, the mice were sacrificed, and both kidneys were harvested and cut into two sagittal sections. One section of each kidney was fixed in formalin, and the other section was snap frozen in liquid nitrogen and stored at −80°C.

2.3.2 Immunohistology—Formalin-fixed kidney samples were embedded with paraffin, cut into 5-μm sections and mounted on slides. Slides were then deparaffinized and rehydrated from xylene through a graded ethanol series to distilled H$_2$O. For specific staining, slides were subsequently processed as described below. Following staining, cover slips were secured using Cytoseal 60 mounting medium. Slides were viewed on a Nikon Eclipse E600 microscope (Nikon Instruments, Melville, NY, USA) and analyzed with an Olympus DP70 camera and software (Olympus Corporation, Tokyo, Japan).

Interstitial renal fibrosis was assessed using picrosirius red staining. Picrosirius red solution was prepared using 0.5 g Sirius red (Sigma-Aldrich Cat. #365548, St. Louis, MO, USA) in 500 mL saturated aqueous solution of picric acid (Sigma-Aldrich Cat. #P6744-1GA). Slides were placed in Wiegert's hematoxylin and stained for 8 min, and then washed for 10 min in running tap water. The slides were then placed in picrosirius red for 60 min, followed by two changes of 0.5% acetic acid. Slides were dehydrated through an ethanol series and cleared in xylene.

Enzymatic antigen retrieval was performed using Proteinase K (Agilent Cat. #S3020, Santa Clara, CA, USA) for 5 min at 37°C. Mouse macrophages were stained using F4/80 (ThermoFisher Cat. #14–4801-82, Waltham, MA, USA) at 1: 500 Overnight (O/N) at 4°C. Slides were subsequently stained with an Anti Rat Horseradish peroxidase (HRP) detection system (ImmPRESS Reagent Kit, Vector Labs Cat. #MP-7444) at room temperature for 35 min. ImmPACT 3,3'-Diaminobenzidine (DAB) (Vector Labs Cat. #SK-4105, Burlingame, CA, USA) was used as an HRP substrate to detect F4/80 and to stain brown. Slides were washed in distilled water, counter-stained with hematoxylin and dehydrated through an ethanol series and cleared in xylene.

2.3.3 Kidney and serum lactate dehydrogenase (LDH)—Snap frozen kidney sections were pulverized into a freeze-dried powder under liquid nitrogen. Protein was extracted from approximately 0.03–0.07 mg of tissue in 150–350 μL cold assay buffer. Samples were centrifuged at 18078 x g at 4°C for 15 min. Supernatants were collected and

assayed for LDH activity (Abcam Cat #ab102526, Cambridge, MA, USA) at a dilution of 1: 500. Serum samples were diluted 1: 500 in assay buffer. All samples were run against a 12.5–2.5 nmol NADH (reduced form of nicotinamide adenine dinucleotide) standard curve measured at an optical density (OD) of 450 nm.

2.3.4 Urine L-lactate—Urine samples collected prior to each imaging examination were deproteinated and centrifuged at 4°C. Supernatants were collected and assayed for lactate (Cayman Cat. #700510, Ann Harbor, MI, USA) without dilution. All samples were run against a 1000–2.5 μmol standard curve at an OD of 540 nm.

2.4 Image analysis

2.4.1 Renal pelvis volume—All image analysis was performed using MATLAB 2014b (The Mathworks, Natick, MA, USA). The severity of the obstruction was assessed on the basis of the degree of hydronephrosis, or fluid accumulation, in the renal pelvis. The renal pelvis volume was calculated using 3D SPGR images viewed in the coronal plane. Images were pre-processed with histogram equalization to correct for spatial variation in signal, and smoothed using a non-local means filter.[17] The renal pelvis was then segmented from other anatomy using k-means clustering of the voxel intensity values (built-in MATLAB function "kmeans" with $k = 2$), followed by manual editing as necessary. The total volume was calculated as the product of the number of segmented voxels and the voxel volume.

2.4.2 Pyruvate and lactate dynamics—Regions of interest (ROIs) for both kidneys, as well as the major vessels (aorta and vena cava), were determined from the 3D anatomic images viewed in the axial plane. For each examination, a maximum intensity projection (MIP) was calculated from 3D SPGR images spanning the 10-mm axial extent of the ^{13}C images. ROIs were drawn manually on the MIP, and then down-sampled to match the spatial resolution of the ^{13}C images. Finally, any portion of each kidney ROI which overlapped with the vessel ROI was excluded in order to mitigate partial volume contamination from the vascular ^{13}C signal. Final ROIs for each kidney included at least 196 pixels.

^{13}C–Pyruvate and ^{13}C–lactate images of the kidney were reconstructed from the spiral k-space data, measured trajectories and field map using an iterative least-squares estimation technique, as described previously.[18] Metabolites other than pyruvate and lactate (e.g. alanine and urea) were not included in the reconstruction model because of the negligibly low signal-to-noise ratio observed for these species in the spectral data. Metabolite flux was quantified using a model-free ratiometric method.[19] Briefly, the complex images were integrated over time to produce maps of the area under the curve (AUC), followed by a magnitude transformation. The average AUC value within each kidney ROI was calculated for pyruvate (AUC_P) and lactate (AUC_L), after which the ratio of these quantities was calculated ($AUC_{ratio} = AUC_L/AUC_P$). AUC_{ratio} has been shown to be linearly proportional to the forward pyruvate to lactate reaction rate constant, and so this quantity was used as a proxy for the assessment of the kinetics of this conversion.

2.5 Statistical analysis

All statistical analysis was performed using R version 2.15.3 (www.r-project.org). Baseline data were analyzed independently of longitudinal data following obstruction, using a paired Student's *t*-test to test for differences between left and right kidneys. Longitudinal data were analyzed by linear mixed effects modeling using the nlme package.[20] Fixed effects included the kidney (left or right) and time post-obstruction (3, 7 or 14 days), whereas random effects included the mouse identifier (numbers 1–9 assigned to each mouse) and the slope between time points. The data for renal pelvis volume, AUC_P and AUC_L were analyzed using a model that included a kidney × time interaction effect. Because we did not observe a significant interaction effect for AUC_{ratio}, these data were analyzed with a simpler model which included only main effects.[21] Statistical significance for all tests was defined as *p* 0.05.

3 RESULTS

3.1 Imaging

Image data were successfully collected in six to nine of the mice at each time point. The sample size varied as a result of a combination of animal attrition and technical failure, as summarized in Table 1. No complications of pUUO surgery, such as infection, were observed and attrition was not directly attributable to pUUO surgery.

Example images, together with AUC_P and AUC_L maps, for a single mouse are shown in Figure 2 to demonstrate the image quality and qualitative characteristics. The left kidney developed significant hydronephrosis by the day 14 time point, visible in the T_2-weighted images. Robust and well-localized pyruvate and lactate signals were detected in both kidneys at baseline, but the signals for both metabolites were markedly decreased in the left kidney by day 14. The pyruvate signal was also observed in the central blood vessels (aorta and vena cava) at all time points, but no significant vascular lactate signal was observed.

A significant kidney × time interaction between left and right renal pelvis volume was found for all time points with respect to baseline (Figure 3A). In addition, the rate of hydronephrosis growth in the left kidney increased with time. Although the total volume of the obstructed kidney increased with progression of hydronephrosis, no obvious changes in the total volume of the contralateral kidney were noted.

AUC_P, the integrated signal for pyruvate, was significantly greater in the right kidney than in the left kidney at baseline ($p = 0.006$; Figure 3B), indicating a systematic difference between kidneys in healthy mice. A significant kidney × time interaction between left and right was observed for the baseline–day 3 and baseline–day 14 intervals, indicating that AUC_P decreased to a greater extent in the left kidney than in the right kidney.

Like AUC_P, baseline AUC_L was significantly greater in the right kidney relative to the left ($p = 0.004$; Figure 3C). Following surgical obstruction, AUC_L increased in the right kidney, but decreased in the left, with significant kidney × time interaction observed for all intervals with respect to baseline.

AUC$_{ratio}$ was not different at baseline for left and right kidneys (Figure 3D). No interaction effects were observed. AUC$_{ratio}$ for all kidneys, obstructed and contralateral, increased significantly at all time points relative to baseline ($p < 0.01$ for each time point).

3.2 Immunohistological and biochemical markers

Figure 4 shows examples of picrosirius red and F4/80 staining for obstructed and contralateral kidneys at day 14. Picrosirius red staining was significantly greater in the obstructed kidney ($p < 0.001$; Figure 5A), indicating increased fibrosis relative to the contralateral kidney. F4/80 staining was also significantly greater in the obstructed kidneys ($p = 0.01$), consistent with a higher level of macrophage infiltration. No difference in LDH activity was observed between kidneys. Whole-body measures of serum LDH activity and urine lactate concentration showed no significant changes across time points (Figure 5B, C).

4 DISCUSSION

In this study, we demonstrated the feasibility of using hyperpolarized [1-^{13}C]pyruvate MRI to investigate UTO, and identified changes in pyruvate handling by both the contralateral and obstructed kidneys. Hyperpolarized ^{13}C MRI may therefore provide unique opportunities for the investigation, regionally and *in vivo*, of the development and progression of UTO, which are not possible with global serum and urine biomarkers or with more invasive methods.

In the obstructed kidney, we observed a decrease in AUC$_P$ and AUC$_L$ and an increase in AUC$_{ratio}$, relative to baseline, at days 3–14. The decline in AUC$_L$ indicates less total lactate production; however, the parallel decline in AUC$_P$ is consistent with reduced perfusion. Indeed, decreased renal blood flow following complete or partial UUO has been reported in a number of studies.[22,23] However, changes in blood flow alone cannot explain the observed increase in AUC$_{ratio}$ following obstruction. Furthermore, because a supraphysiological concentration of pyruvate was injected, it seems unlikely that intravascular pyruvate availability was the limiting factor for conversion to lactate, even after taking perfusion changes into account. Several studies in cancer cell lines have indicated that control of label flux from ^{13}C–pyruvate to ^{13}C–lactate is shared between the membrane transporter, endogenous lactate and LDH activity.[24–26] In our data, urine LDH concentration and serum activity were constant over the duration of the study, suggesting that downstream cellular uptake in response to a metabolic shift towards glycolysis is a plausible explanation for the observed increase in the lactate to pyruvate ratio, as opposed to reduced substrate delivery or large shifts in LDH activity. Meanwhile, the observed decrease in absolute lactate production is probably a result of reduced renal blood flow and glomerular filtration as a consequence of obstruction, based on the expected relationship between filtered load and energy demand in the kidney.[27]

The lactate to pyruvate ratio measured with hyperpolarized ^{13}C MRI is emerging as an interesting potential biomarker in independent studies of mouse and rat models of kidney ischemia–reperfusion injury. Acute injury as a result of a longer duration of ischemia (60 min *versus* 30 min) was associated with a decreased lactate to pyruvate ratio that coincided with reduced cortical tissue LDH activity.[28] The mechanism of injury in the two

experimental models is substantially different: ischemia *versus* obstruction. In contrast with ischemia–reperfusion injury, partial obstructive nephropathy in our study is designed to be a chronic inflammatory and fibrogenetic injury model in which the UUO and contralateral kidneys are adapting to the increased stress and workload required to maintain function. In this chronic injury condition, we speculate that the observed increase in AUC_{ratio} reflects a shift in the relative metabolism from oxidative phosphorylation towards glycolysis, perhaps in response to increased cellular demand to meet the additional functional workload of resorption. This situation is probably exacerbated by the observed decrease in perfusion that could drive metabolism in the cortex further towards anaerobic glycolysis in response to inflammation and hypoxia.[29] Inflammation and fibrotic injury, typical of chronic kidney injury, are supported by our histological results at day 14.

Interestingly, the contralateral non-obstructed kidney also showed a trend towards moderately decreased AUC_P after surgery, together with an increase in both AUC_L and AUC_{ratio}. Somewhat surprisingly, changes in AUC_{ratio} paralleled those of the obstructed kidney, with no significant difference between left and right observed. The increase in AUC_L could indicate greater absolute lactate production, possibly as a general compensatory response to the reduced function of the obstructed kidney. It is not necessarily surprising to see a comparable increase in AUC_{ratio} after obstruction for the right, unobstructed, kidney as a compensatory effect to offset the loss of function in the left. Moreover, given this apparent compensatory metabolic effect, the observation of comparable lactate concentration in the urine before and after obstruction, as summarized in Figure 5, is also not surprising, as an indicator of comparable global output before and after obstruction.

Overall, these results may be caused by a systemic or hormonal response which affects both kidneys following unilateral obstruction. One candidate for this is the renin–angiotensin system, which is well known to be activated in UTO.[30] Amongst other functions, angiotensin II enhances sodium reabsorption by the renal tubules. It is therefore possible that a component of the metabolic response in the contralateral kidney can be attributed to the renin–angiotensin system. Targeted studies to specifically test this hypothesis in the context of renal disease are necessary.

It is worth noting that the apparent rate of pyruvate to lactate conversion, as well as its proxy AUC_{ratio}, depend not only on LDH activity, but also on the cellular uptake of pyruvate via monocarboxylate transport proteins (MCTs). Which of these is the rate-limiting step is an open question in the context of hyperpolarized ^{13}C imaging,[26] and the answer probably depends on the particular organ system and disease state under study. We observed no significant difference in LDH activity between right and left kidneys harvested at day 14; however, this is far from definitive evidence of MCTs as rate-limiting, and further investigation into the biochemical pathways is warranted. In particular, direct measurement of MCT expression and metabolomic analysis of urine, blood or tissue samples by nuclear magnetic resonance (NMR) spectroscopy may provide valuable information complementary to imaging.

Interestingly, the baseline values of AUC_P and AUC_L were systematically greater in the right kidney relative to the left. However, AUC_{ratio} did not show differences at baseline, indicating

a consistent stoichiometric relationship in both kidneys. These results suggest that observed baseline differences may result from asymmetry with respect to renal blood flow rather than LDH or MCT activity. A similar phenomenon has been reported in the context of blood oxygen level-dependent (BOLD) MRI, with the left kidney displaying greater R_2^* than the right in healthy volunteers.[31,32] These observations imply lower oxygenation, which would result from lower blood flow to the left kidney, consistent with our results. The lower blood flow to the left kidney might be attributable to differences in renal vein morphology or mild compression by neighboring abdominal organs.[32,33]

An attractive characteristic compared with other imaging modalities is the ability to combine ^1H and ^{13}C MRI for multiple measures of both anatomy and function. For example, a comprehensive assessment of the kidney may also include renal fibrosis measurements using diffusion-weighted MRI or T_1 mapping.[34–37] Combined imaging of metabolism by hyperpolarized ^{13}C MRI with proton methods could yield important information about the possible interplay and timing between metabolic changes, inflammation and fibrosis that could help to guide the utility of functional MRI of the kidney as a means to monitor renal disease severity and progression.[38]

Along similar lines, studies that independently measure multiple functional parameters may further reveal specific mechanisms contributing to changes in lactate production during kidney injury. For example, dual injection of ^{13}C–pyruvate and ^{13}C–urea can be used to independently probe metabolism and perfusion in the same experiment.[39] Alternatively, both hyperpolarized ^{13}C–pyruvate and ^{13}C–dehydroascorbic acid (DHA), the oxidized form of vitamin C, can be used to study metabolism and redox capacity associated with the underlying cellular environment of kidney injury, including cell stress, chronic inflammation and loss of tubular function.[40] Recent work in a rodent model of ischemia–reperfusion injury has employed such combined strategies with results in general agreement with our study. For example, in a rat model of ischemia–reperfusion injury, hyperpolarized $^{13}C,^{15}N_2$-urea and sodium MRI techniques were employed to demonstrate the corresponding loss of urea and sodium concentration gradients, and therefore tubular injury leading to reduced filtration, in injured *versus* contralateral kidneys.[10]

We acknowledge a number of limitations in this study. First, the choice of kidney to be obstructed was not randomized between right and left. Although the reproducibility of the surgical procedure was probably maximized by obstructing only the left kidney in all cases, this design limits the interpretation of the results. For example, it is possible that changes following obstruction may differ depending on whether the left or right ureter is obstructed. Evidence of systematic differences in AUC_L and AUC_P at baseline further highlights the need to randomize the treatment effect in studies which utilize one kidney as a control. Second, although we excluded the ^{13}C signal from the large central vessels in our analysis, we were unable to distinguish between intravascular and intracellular contributions within the kidney body. This may introduce errors in the quantitative relationship between the pyruvate and lactate signals, as the AUC analysis is based on a one-compartment, two-pool exchange.[41] This has been a challenge for hyperpolarized ^{13}C MRI in general, and new methods for vascular suppression are being developed which may mitigate this, such as the use of bipolar gradients,[42] double spin-echo[42] and gadolinium-based contrast agents.[43] An

additional solution would be to co-inject a blood-pool hyperpolarized compound, such as ^{13}C–urea, with ^{13}C–pyruvate for an independent, but simultaneous, measure of blood flow.[44] Third, as a result of the natural interdependence between the left and right kidney, the inclusion of a sham operation as a control group would have been of value as a negative control to eliminate possible changes caused by non-specific processes on the obstructed side, such as inflammation. Fourth, the duration of overnight fasting was substantial. However, this duration was logistically necessary, and fasting was important to minimize blood glucose variability.[45] Finally, we note that the UUO model represents a pronounced injury with obvious changes in kidney morphology and function in response. Although cases of severe UTO in patients are similarly detected by conventional MRI or ultrasound, the variability of UTO presentation across patients remains a challenge for these approaches. Given the association of metabolic markers with UTO, it is not unreasonable to explore the potential role of metabolism in assessing the progression of kidney injury in the UUO model. Therefore, the UUO model, whilst extreme compared with the variability encountered in UTO, nonetheless provides a means to establish the feasibility of hyperpolarized ^{13}C–pyruvate MRI to assess severity and progression in UTO. For example, in UTO, we anticipate that obstruction may be intermittent or of a functional rather than a structural basis, and so anatomical images may not always appear as obvious as those shown in Figure 2 for the UUO model.

5 CONCLUSIONS

We identified *in vivo* alterations in renal pyruvate and lactate metabolism in both obstructed and contralateral kidneys following pUUO. The obstructed kidney showed associated and expected development of hydronephrosis, interstitial fibrosis and infiltration of macrophages at sacrifice, whereas the contralateral kidney did not. The results suggest that hyperpolarized ^{13}C MRI may provide a valuable non-invasive tool for the assessment of regional changes in metabolism caused by kidney injury.

Acknowledgments

Abbreviations used

2D/3D	two-/three-dimensional
AUC	area under the curve
AUC$_L$	area under the lactate *versus* time curve
AUC$_P$	area under the pyruvate *versus* time curve
AUC$_{ratio}$	ratio of AUC$_L$ to AUC$_P$

BOLD	blood oxygen level-dependent
DAB	3,3'-Diaminobenzidine
DHA	dehydroascorbic acid
FSE	fast spin echo
LDH	lactate dehydrogenase
MCT	monocarboxylate transport protein
MIP	maximum intensity projection
MRI	magnetic resonance imaging
NADH	reduced form of nicotinamide adenine dinucleotide
NMR	nuclear magnetic resonance
OD	optical density
pUUO	partial unilateral ureteral obstruction
ROI	region of interest
SPGR	spoiled gradient echo sequence
UTO	urinary tract obstruction
UUO	unilateral ureteral obstruction

References

1. [Accessed October 12, 2016] North American pediatric renal trials and collaborative studies annual report. 2014. https://web.emmes.com/study/ped/index.htm

2. Chevalier RL, Forbes MS, Thornhill BA. Ureteral obstruction as a model of renal interstitial fibrosis and obstructive nephropathy. Kidney Int. 2009; 75(11):1145–1152. [PubMed: 19340094]

3. Yoshioka Y, Tsutsumi T, Adachi M, Tokumura A. Altered phospholipid profile in urine of rats with unilateral ureteral obstruction. Metabolomics. 2009; 5(4):429–433.

4. MacLellan DL, Mataija D, Doucette A, et al. Alterations in urinary metabolites due to unilateral ureteral obstruction in a rodent model. Mol Biosyst. 2011; 7(7):2181–2188. [PubMed: 21547298]

5. Zhang H, Jia J, Cheng J, Ye F, Li X, Gao H. ^{1}H NMR-based metabonomics study on serum of renal interstitial fibrosis rats induced by unilateral ureteral obstruction. Mol Biosyst. 2012; 8(2):595–601. [PubMed: 22027911]

6. Dong BJ, Jia JM, Hu WY, et al. Application of H-1 NMR metabonomics in predicting renal function recoverability after the relief of obstructive uropathy in adult patients. Clin Biochem. 2013; 46(4–5): 346–353. [PubMed: 23195136]

7. Clatworthy MR, Kettunen MI, Hu DE, et al. Magnetic resonance imaging with hyperpolarized [1,4-(13C2]fumarate allows detection of early renal acute tubular necrosis. Proc Natl Acad Sci U S A. 2012; 109(33):13374–13379. [PubMed: 22837393]

8. Laustsen C, Lycke S, Palm F, et al. High altitude may alter oxygen availability and renal metabolism in diabetics as measured by hyperpolarized [1-(13C)] pyruvate magnetic resonance imaging. Kidney Int. 2014; 86(1):67–74. [PubMed: 24352155]

9. Laustsen C, Ostergaard JA, Lauritzen MH, et al. Assessment of early diabetic renal changes with hyperpolarized [1-(13)C]pyruvate. Diabetes Metab Res Rev. 2013; 29(2):125–129. [PubMed: 23166087]

10. Nielsen PM, Hansen ESS, Norlinger TS, et al. Renal ischemia and reperfusion assessment with three-dimensional hyperpolarized C-13, (15)N$_2$-urea. Magn Reson Med. 2016; 76(5):1524–1530. [PubMed: 27548739]

11. von Morze C, Bok RA, Sands JM, Kurhanewicz J, Vigneron DB. Monitoring urea transport in rat kidney in vivo using hyperpolarized (1)(3)C magnetic resonance imaging. Am J Physiol Renal Physiol. 2012; 302(12):F1658–F1662. [PubMed: 22492940]

12. Xu T, Mayer D, Gu M, et al. Quantification of in vivo metabolic kinetics of hyperpolarized pyruvate in rat kidneys using dynamic ^{13}C MRSI. NMR Biomed. 2011; 24(8):997–1005. [PubMed: 21538639]

13. von Morze C, Chang GY, Larson PEZ, et al. Detection of localized changes in the metabolism of hyperpolarized gluconeogenic precursors C-13-lactate and C-13-pyruvate in kidney and liver. Magn Reson Med. 2017; 77(4):1429–1437. [PubMed: 27098724]

14. Laustsen C, Nielsen PM, Norlinger TS, et al. Antioxidant treatment attenuates lactate production in diabetic nephropathy. Am J Physiol Renal Physiol. 2017; 312(1):F192–F199. [PubMed: 28069660]

15. Duyn JH, Yang Y, Frank JA, van der Veen JW. Simple correction method for k-space trajectory deviations in MRI. J Magn Reson. 1998; 132(1):150–153. [PubMed: 9615415]

16. Gurney, P., Pauly, J., Nishimura, D. A simple method for measuring B0 eddy currents. Proceedings of the 13th Annual Meeting ISMRM; Miami, FL, USA. 2005.

17. Buades, A., Coll, B., Morel, JM. A non-local algorithm for image denoising. Proceedings of the 2005 IEEE Computer Society Conference on Computer Vision and Pattern Recognition; San Diego, CA, USA. 2005.

18. Gordon, J., Fain, S., Johnson, K. Direct estimation of hyperpolarized metabolites with IDEAL spiral CSI. Proceedings of the 20th Annual Meeting ISMRM; Melbourne, Australia. 2012.

19. Hill DK, Orton MR, Mariotti E, et al. Model free approach to kinetic analysis of real-time hyperpolarized ^{13}C magnetic resonance spectroscopy data. PLoS One. 2013; 8(9):e71996. [PubMed: 24023724]

20. R Core Team. NLME: Linear and Nonlinear Mixed Effects Models. 2012. https://www.r-project.org

21. Brambor T, Clark WR, Golder M. Understanding interaction models: improving empirical analyses. Polit Anal. 2006; 14(1):63–82.

22. Vaughan ED Jr, Marion D, Poppas DP, Felsen D. Pathophysiology of unilateral ureteral obstruction: studies from Charlottesville to New York. J Urol. 2004; 172(6 Pt 2):2563–2569. [PubMed: 15538209]

23. Wen JG. Partial unilateral ureteral obstruction in rats. NeurourolUrodyn. 2002; 21(3):231–250.

24. Harris T, Eliyahu G, Frydman L, Degani H. Kinetics of hyperpolarized C-13(1)-pyruvate transport and metabolism in living human breast cancer cells. Proc Natl Acad Sci U S A. 2009; 106(43):18131–18136. [PubMed: 19826085]

25. Kettunen MI, Hu DE, Witney TH, et al. Magnetization transfer measurements of exchange between hyperpolarized [1-C-13]pyruvate and [1-C-13]lac-tate in a murine lymphoma. Magn Reson Med. 2010; 63(4):872–880. [PubMed: 20373388]

26. Witney TH, Kettunen MI, Brindle KM. Kinetic modeling of hyperpolarized C-13 label exchange between pyruvate and lactate in tumor cells. J Biol Chem. 2011; 286(28):24572–24580. [PubMed: 21596745]

27. Brezis M, Heyman SN, Epstein FH. Determinants of intrarenal oxygenation. II. Hemodynamic effects. Am J Physiol. 1994; 267(6 Pt 2):F1063–F1068. [PubMed: 7810693]

28. Nielsen PM, Laustsen C, Bertelsen LB, et al. In situ lactate dehydrogenase activity: a novel renal cortical imaging biomarker of tubular injury? Am J Physiol Renal Physiol. 2017; 312(3):F465–F473. [PubMed: 27654895]

29. Haque ME, Franklin T, Bokhary U, et al. Longitudinal changes in MRI markers in a reversible unilateral ureteral obstruction mouse model: preliminary experience. J Magn Reson Imaging. 2014; 39(4):835–841. [PubMed: 24151096]

30. Klahr S, Morrissey J. Obstructive nephropathy and renal fibrosis. Am J Physiol Renal Physiol. 2002; 283(5):F861–F875. [PubMed: 12372761]

31. Niles DJ, Artz NS, Djamali A, Sadowski EA, Grist TM, Fain SB. Longitudinal assessment of renal perfusion and oxygenation in transplant donor–recipient pairs using arterial spin labeling and blood oxygen level-dependent magnetic resonance imaging. Invest Radiol. 2016; 51(2):113–120. [PubMed: 26561047]

32. Simon-Zoula SC, Hofmann L, Giger A, et al. Non-invasive monitoring of renal oxygenation using BOLD-MRI: a reproducibility study. NMR Biomed. 2006; 19(1):84–89. [PubMed: 16411163]

33. Kurklinsky AK, Rooke TW. Nutcracker phenomenon and nutcracker syndrome. Mayo Clin Proc. 2010; 85(6):552–559. [PubMed: 20511485]

34. Cai XR, Yu J, Zhou QC, Du B, Feng YZ, Liu XL. Use of intravoxel incoherent motion MRI to assess renal fibrosis in a rat model of unilateral ureteral obstruction. J Magn Reson Imaging. 2016; 44(3):698–706. [PubMed: 26841951]

35. Friedli I, Crowe LA, Berchtold L, et al. New magnetic resonance imaging index for renal fibrosis assessment: a comparison between diffusion-weighted imaging and T1 mapping with histological validation. Sci Rep. 2016; 6:30088. https://doi.org/10.1038/srep30088. [PubMed: 27439482]

36. Hennedige T, Koh TS, Hartono S, et al. Intravoxel incoherent imaging of renal fibrosis induced in a murine model of unilateral ureteral obstruction. Magn Reson Imaging. 2015; 33(10):1324–1328. [PubMed: 26248270]

37. Togao O, Doi S, Kuro-o M, Masaki T, Yorioka N, Takahashi M. Assessment of renal fibrosis with diffusion-weighted MR imaging: study with murine model of unilateral ureteral obstruction. Radiology. 2010; 255(3):772–780. [PubMed: 20406881]

38. Zhang JL, Morrell G, Rusinek H, et al. New magnetic resonance imaging methods in nephrology. Kidney Int. 2014; 85(4):768–778. [PubMed: 24067433]

39. Bahrami N, Swisher CL, Von Morze C, Vigneron DB, Larson PE. Kinetic and perfusion modeling of hyperpolarized (13)C pyruvate and urea in cancer with arbitrary RF flip angles. Quant Imaging Med Surg. 2014; 4(1):24–32. [PubMed: 24649432]

40. Baligand, C., Qin, H., True-Yasaki, A., et al. Hyperpolarized ^{13}C magnetic resonance evaluation of renal ischemia reperfusion injury in a murine model. Proceedings of the 25th Annual Meeting ISMRM; Honolulu, HI. 2017.

41. Day SE, Kettunen MI, Gallagher FA, et al. Detecting tumor response to treatment using hyperpolarized C-13 magnetic resonance imaging and spectroscopy. Nat Med. 2007; 13(12):1382–1387. [PubMed: 17965722]

42. Gordon JW, Niles DJ, Adamson EB, Johnson KM, Fain SB. Application of flow sensitive gradients for improved measures of metabolism using hyperpolarized (13)C MRI. Magn Reson Med. 2016; 75(3):1242–1248. [PubMed: 25951611]

43. Smith MR, Peterson, Gordon JW, et al. In vivo imaging and spectroscopy of dynamic metabolism using simultaneous ^{13}C and ^{1}H MRI. IEEE Trans Biomed Eng. 2012; 59(1):45–49. [PubMed: 21775254]

44. von Morze C, Bok RA, Reed GD, Ardenkjaer-Larsen JH, Kurhanewicz J, Vigneron DB. Simultaneous multiagent hyperpolarized C-13 perfusion imaging. Magn Reson Med. 2014; 72(6):1599–1609. [PubMed: 24382698]

45. Serrao EM, Rodrigues TB, Gallagher FA, et al. Effects of fasting on serial measurements of hyperpolarized [1-C-13]pyruvate metabolism in tumors. NMR Biomed. 2016; 29(8):1048–1055. [PubMed: 27309986]
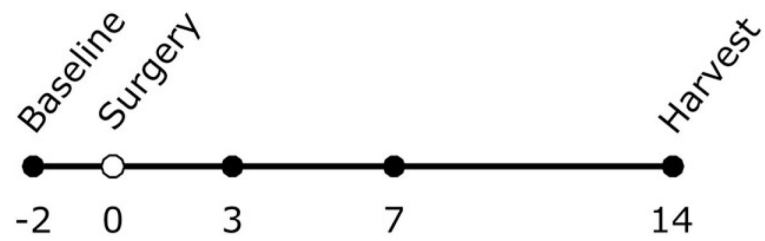
FIGURE 1.

Experimental time line for each mouse. Partial unilateral ureteral obstruction (pUUO) surgery was performed at day 0 (open circle). Magnetic resonance imaging and collection of blood and urine samples were performed 2 days prior to surgery (baseline) and at three separate time points afterwards (filled circles). After imaging on the final day, mice were sacrificed and both kidneys were harvested for immunohistological and biochemical evaluation
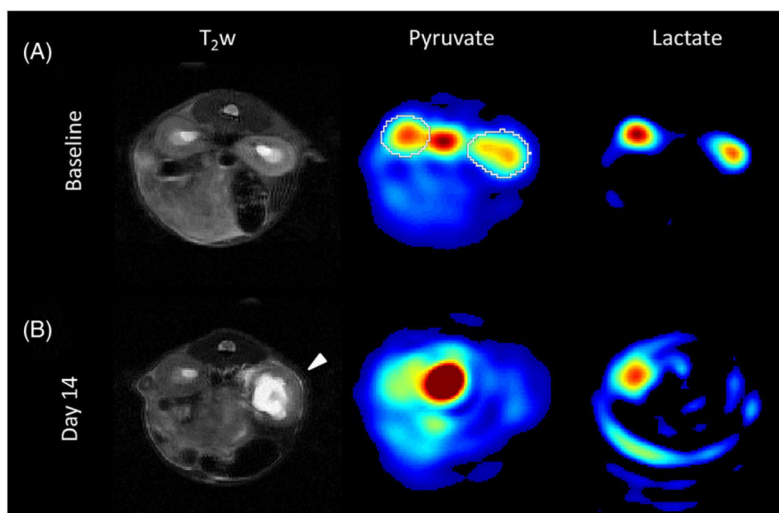
FIGURE 2.
Comparison of axial ^{1}H and ^{13}C images before and after partial ureteral obstruction. (A) Kidneys appear normal in the T_2-weighted (T$_2$w) image, and both pyruvate and lactate are detected in both kidneys at baseline. (B) At 14 days following obstruction, hydronephrosis is apparent in the left kidney (arrow), accompanied by a marked reduction in the pyruvate and lactate signal in this kidney. Image scaling is equivalent across (A) and (B) for pyruvate and lactate. An example region of interest is overlaid on the baseline pyruvate image (white)
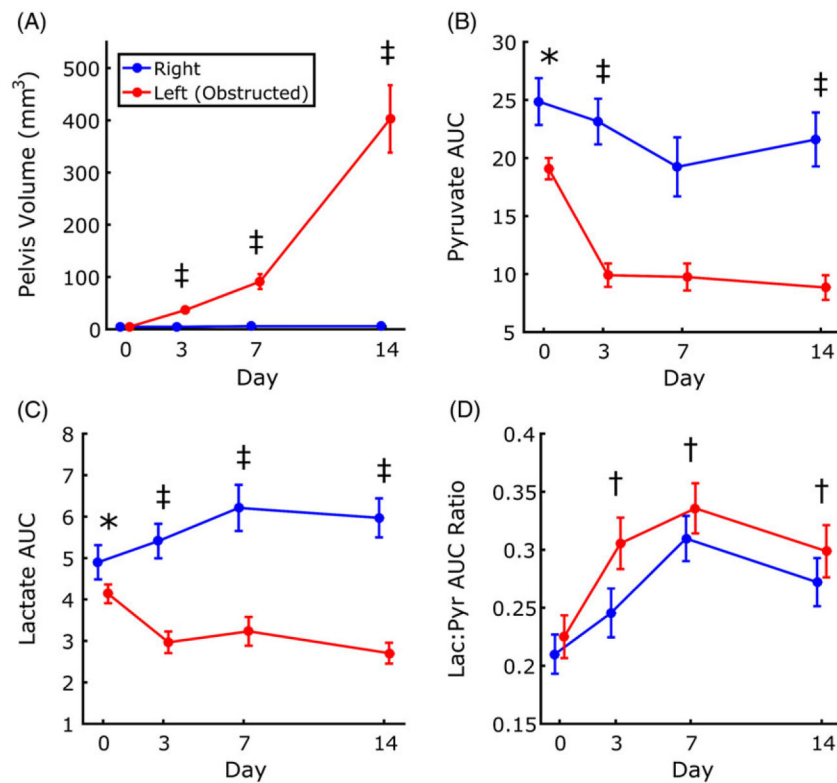
FIGURE 3.
Changes in renal pelvis volume, lactate and pyruvate across time points. Significant interaction effects at multiple time points were found for renal pelvis volume (A), pyruvate area under the curve (AUC) (B) and lactate AUC (C). Pyruvate AUC and lactate AUC also showed significant differences between left and right at baseline. The ratio of lactate and pyruvate AUC did not show differences between kidneys, but showed significant changes with respect to baseline (D). Data are plotted as mean ± standard error. *p 0.05 between left and right kidneys; †p 0.05 for main effect with respect to baseline; ‡p 0.05 for kidney × time interaction effect with respect to baseline
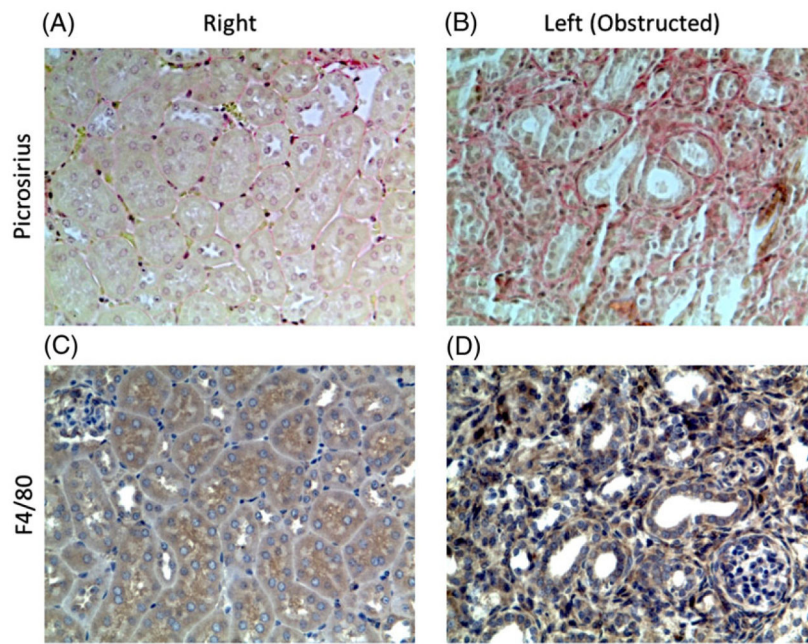
FIGURE 4.

Picrosirius red (A, B) and F4/80 (C, D) immunohistological staining of kidney sections. The increased density of red pigment in (B) relative to (A) indicates greater collagen deposition, or fibrosis. Similarly, the increased density of the blue pigment in (D) relative to (C) indicates greater infiltration by macrophages
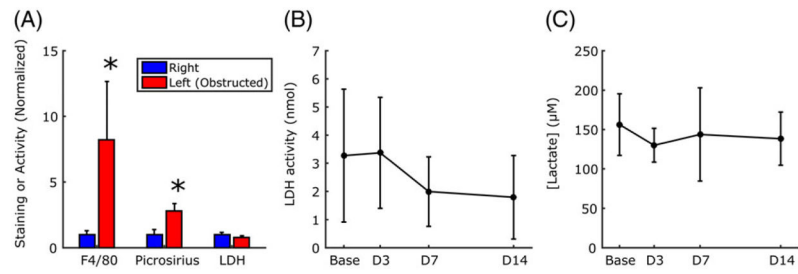
FIGURE 5.
Quantitative comparison of immunohistological and biochemical assay results. Significantly greater intensity of staining was found in the left kidney relative to the right for both F4/80 and picrosirius red, although the activity of lactate dehydrogenase (LDH) in the kidneys was not different (A). LDH activity in the serum (B) and lactate concentration in the urine (C) showed no significant changes across time points. In (A), data are normalized to the value of the right kidney. Data are plotted as mean ± standard deviation. *p 0.05 between left and right kidneys

TABLE 1

Sample sizes for the acquired data at each time point

Time point	Sample size	Reason for missing data (number of mice affected)
Baseline	8	Inadequate polarization (1)
Day 3	9	N/A
Day 7	6	Attrition (2); technical failure (1)
Day 14	6	Attrition (1)